International Journal of Nanomedicine

Dovepress
Taylor & Francis Group

Open Access Full Text Article

ORIGINAL RESEARCH

Optimizing Triple-Negative Breast Cancer Therapy via Ultrasound-Enhanced Piezocatalysis for Targeted Chemodrug Release

Qingwen Xue[1,*], Ningning He[2,*], Yuxiu Gao[1], Xuehui Zhang[1], Shuao Li[1], Fang Chen[1], Chunping Ning[1], Xiaoyu Wu[2], Jingtong Yao[2], Ziheng Zhang[2], Shangyong Li[1,2], Cheng Zhao[1]

[1]Department of Ultrasound, the Affiliated Hospital of Qingdao University, Qingdao, 266003, People's Republic of China; [2]School of Basic Medicine, Qingdao Medical College, Qingdao University, Qingdao, 266003, People's Republic of China

*These authors contributed equally to this work

Correspondence: Cheng Zhao; Shangyong Li, Email zhaochengdr@163.com; lisy@qdu.edu.cn

Introduction: Triple-negative breast cancer (TNBC) is known for its high malignancy, limited clinical treatment options, and poor chemotherapy outcomes. Although some advancements have been made using nanotechnology-based chemotherapy for TNBC treatment, the controlled and on-demand release of chemotherapeutic drugs at the tumor site remains a challenge.

Methods: We manufactured DOX/$BaTiO_3$@cRGD-Lip (DBRL) nanoparticles as an ultrasound (US)-controlled release platform targeting the delivery of Doxorubicin (DOX) for TNBC treatment. The nanoparticles incorporate DSPE-Se-Se-PEG-NH_2 as the liposomal membrane for ROS responsiveness, cRGD peptide for TNBC cell selectivity, and polyethylene glycol for minimized phagocytic cell absorption.

Results: The DBRL+US group achieved significant tumor inhibition (70.27% compared to control group, $p < 0.001$), while maintaining excellent biocompatibility with over 90% cell viability in normal cells. The selective cytotoxicity was evidenced by a 55.70% cell death rate in 4T1 cancer cells under US activation. DBRL showed enhanced tumor accumulation with peak fluorescence intensity of $(1.01 \pm 0.33)\times10^9$ at 12 hours post-injection.

Conclusion: This targeted nanocomposite material paves a new prospect for future precise piezoelectric catalytic therapy for the treatment of TNBC.

Keywords: sonodynamic therapy, chemotherapy, triple-negative breast cancer, drug delivery, ultrasound

Introduction

Triple-negative breast cancer (TNBC) is acknowledged as a particularly aggressive subtype of breast cancer, characterized by increased mortality rates, rapid metastasis, and accelerated rates of recurrence.[1–3] Although the prognosis of TNBC is not encouraging, numerous studies have revealed that it is more sensitive to chemotherapy than other molecular subtypes.[4–6] Despite some recent advances in targeted therapies, chemotherapy remains the primary clinical treatment option for TNBC patients. However, its effectiveness is significantly hampered by poor drug delivery efficiency, severe systemic side effects, and the development of drug resistance. Doxorubicin (DOX) (commercial name: Adriamycin) is a widely-used anthracycline medication, occupying an essential role in the treatment regimen for TNBC.[7] Despite its frequent use, a significant issue with the administration of DOX is its adverse effects, particularly on cardiac function, myelosuppression, alopecia, and hepatic toxicity.[8–10] Simultaneously, the lack of specificity in antitumor drugs causes great damage to healthy human cells, while the inability to concentrate the therapeutic dose in the vicinity of the tumor leads to its resistance.[11,12] Remarkable advances in reducing side effects have been made through the use of a targeted chemotherapy method that employs a liposomal system, such as Doxil® (Johnson & Johnson, Piscataway, NJ).[13] Nevertheless, its safety remains under close examination due to the adverse effects that patients have experienced.[14]

Received: 9 November 2024
Accepted: 23 February 2025
Published: 6 March 2025

Hence, it is imperative to advance the development of augmented DOX delivery systems for devising effective therapeutic strategies to combat TNBC.

Liposomal drug delivery systems are an ideal platform for combining multiple strategies, particularly when it comes to TNBC treatment.[15] When the surfaces of liposomes are modified with polyethylene glycol (PEG), there is a decrease in their nonspecific binding to plasma proteins, diminishing the likelihood of rapid recognition and clearance by the reticuloendothelial system (RES).[16] This enhances the probability of their reaching tumor tissues, via passive or active targeting mechanisms. Leveraging both passive and active targeting mechanisms, the incorporation of chemotherapeutic drugs into liposomes can enhance their specificity towards malignant cells, thus reducing the harm inflicted upon normal cells. Passive targeting in oncological treatments utilizes the enhanced permeation and retention (EPR) effect, wherein nanoparticles (NPs) take advantage of the inadequately developed and permeable vasculature characteristic of swiftly proliferating tumors to accumulate preferentially at tumor locations.[17–19] Although passive targeting holds promise in cancer therapy, two primary challenges persist: the lack of precise control over cellular uptake of liposomal drug delivery systems and the variability in EPR effects among different tumor types. In comparison, active targeting strategy makes use of particular ligands to enhance the absorption of liposomes by breast cancer cells, particularly for directing delivery to the exact tumor site where the EPR does not function.[20,21] The arginine-glycine-aspartic acid (RGD) sequence, particularly cyclic RGD (cRGD), is of great importance in cellular recognition and binding, making it a viable option for active targeting of tumors in oncological therapy.[22,23] Another method is to create liposomes that respond to external stimuli, such as reactive oxygen species (ROS)-responsive liposomes.[24]

ROS-responsive liposomes represent a significant advancement over conventional drug delivery systems. These smart carriers can specifically release their therapeutic payload in response to elevated ROS levels in the tumor microenvironment, enabling precise drug delivery. The system achieves a dual therapeutic effect through both chemotherapy drug release and ROS-mediated tumor cell destruction, creating a synergistic anti-tumor response. The release kinetics can be finely tuned by adjusting ultrasound (US) parameters, providing unprecedented control over drug delivery. Traditional drug carriers often lack this level of intelligent responsiveness and precise control, leading to premature drug release or uneven distribution. Furthermore, ROS-responsive liposomes are constructed from biocompatible materials, minimizing systemic toxicity while maintaining therapeutic efficacy. This combination of targeted delivery, controlled release, and enhanced safety profile makes ROS-responsive liposomes particularly promising for TNBC treatment, addressing many limitations of conventional delivery systems.

Sonodynamic therapy (SDT) shows promise as a minimally invasive treatment option with fewer side effects, offering enhanced potential for the treatment of cancer.[25,26] Barium titanate (BT), a quintessential piezoelectric acoustic sensitizer, is known to produce ROS under ultrasonic stimulation through the reaction of charge carriers it generates with surrounding molecular H_2O and O_2.[27–31] US activated barium titanate nanoparticles (BTNPs) generate cytotoxic ROS to eradicate cancer cells, while ensuring the safety of normal tissues not subjected to US. Consequently, ROS-responsive liposomes that guarantee efficient simultaneous delivery of BTNPs and DOX, coupled with a reduction in the collateral toxicity of DOX, offer considerable promise in the realm of cancer therapy. ROS generated by SDT can effectively destroy cancer cells through necrosis or apoptosis, and most importantly, instigate the precise release of DOX for targeted chemotherapy. Notably, US stands out for its unparalleled spatial-temporal selectivity and superior tissue penetration, positioning SDT as the most promising technology for the future.[32]

In this study, we have engineered ROS-responsive liposomes modified with PEG and featuring a "Se-Se" structure. We innovatively incorporates BTNPs into ROS-sensitive liposomes to achieve controlled drug release. These liposomes have further augmented their targeting capabilities through the integration of cRGD peptides and encapsulate BTNPs and DOX within their vesicles (DOX/BTNPs@cRGD-Lip, DBRL) (Figure 1). In these liposomes, the cRGD peptides are designated for the recognition of TNBC cells, the DOX for chemotherapy, and BTNPs for the generation of ROS to kill cancer cells and control the release of DOX following ultrasonic irradiation. We then proceeded to investigate the precise targeting capability of cRGD peptides, the levels of ROS triggered by SDT, and the combined therapeutic efficacy of DBRL both in vitro and in vivo.

US offers non-invasive deep tissue penetration with precise spatiotemporal control, which is crucial for treating TNBC given its aggressive nature and high metastatic potential. Moreover, TNBC cells demonstrate particular sensitivity

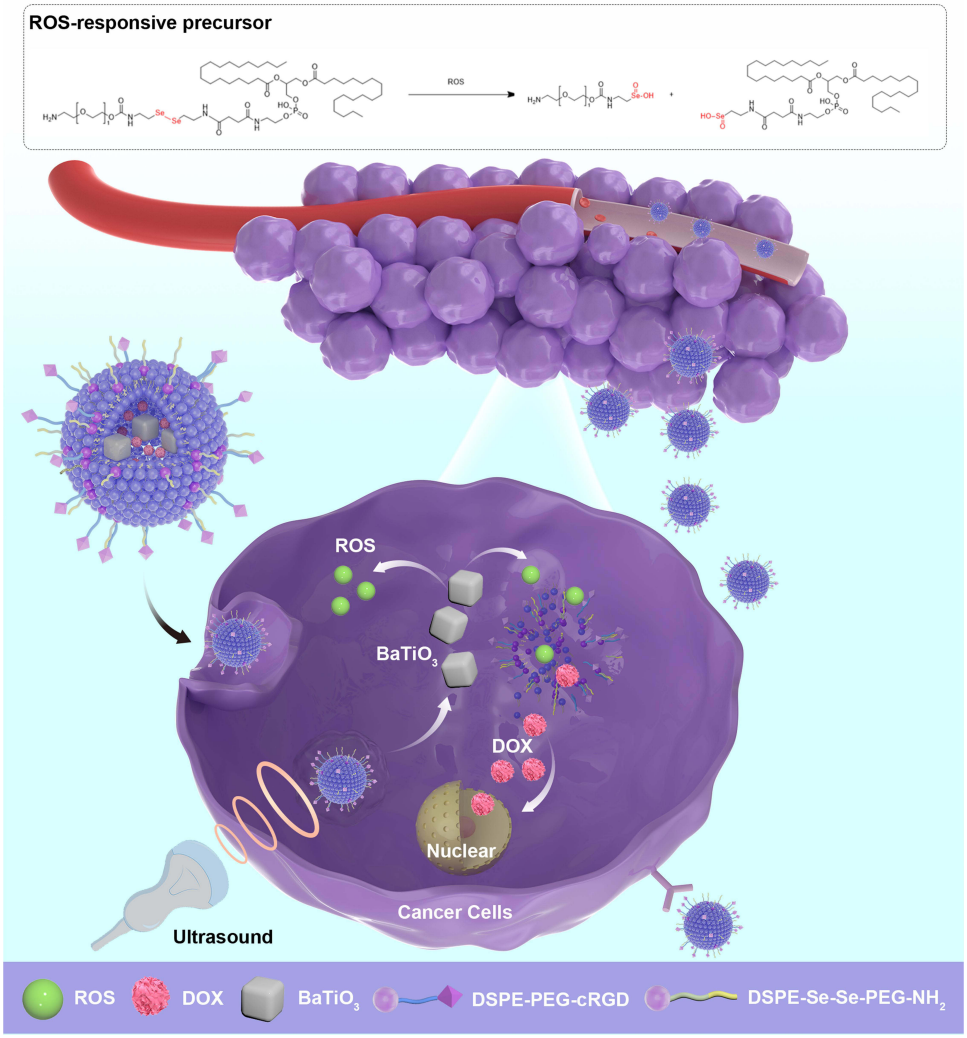

Figure 1 Schematic illustration of the effective tumor chemotherapy with enhancing DOX release through US-triggered piezocatalysis.

to ROS, making the ROS generated through piezocatalysis an effective mechanism for inducing tumor cell apoptosis. The study results indicate that the improved DOX delivery system is highly effective and dependable for targeting chemotherapeutic drug delivery and delivering precise treatment for TNBC.

Experimental Section

Materials

BTNPs was purchased from Beijing Zhongke Yannuo Advanced Materials Technology Co., Ltd. (Beijing, China). 1.3-Diphenylisobenzofuran (DPBF), Dimethyl sulfoxide (DMSO), and Tetrahydrofuran (THF) were purchased from Aladdin Industrial Corporation (Shanghai, China). Hydrogenated soy phosphatidylcholine (HSPC), cholesterol, and DOX were acquired from Shanghai Macklin Biochemical Co., Ltd (Beijing, China). Dihydroethidium (DHE) was purchased from Sigma-Aldrich (St. Louis, USA). DSPE-PEG_{2000}, DSPE-PEG_{2000}-NH_2, DSPE-PEG_{2000}-Cy5.5, DSPE-Se-Se-PEG-NH_2, and DSPE-PEG_{2000}-cRGD were all obtained from RuiXi Co., Ltd (Xian, China). The Hoechst 33342, 4′,6-diamidino-2-phenylindole (DAPI), Cell Counting Kit-8 (CCK-8) Reagent, Propidium iodide and calcein acetoxymethylester (Calcein-AM/PI) Reagent, Annexin V-FITC/PI Apoptosis Detection Kit, and ROS Assay Kit were purchased from Beyotime Biotechnology (Shanghai, China). All chemicals and reagents used in this investigation were analytical grade and used without further purification.

https://doi.org/10.2147/IJN.S505526

Preparation of DBRL Nanoparticles

To prepare the BTNPs dispersion, 20 mg of BTNPs and 24 mg of DSPE-PEG_{2000} were ultrasonically dispersed in 1 mL of THF. The solution was then gradually injected into 10 mL of distilled water under continuous US conditions, followed by an additional 5 minutes of US. The resulting formulation was purified through three rounds of centrifugation with deionized water to remove any remaining lipids and solvent. In 12 mL of chloroform, 17 mg of HSPC, 2 mg of cholesterol, and 5 mg each of DSPE-PEG-cRGD and DSPE-Se-Se-PEG-NH_2 were dissolved. Evaporation of the mixture at 50 °C for 30 minutes with a rotary evaporator resulted in the formation of a lipid film. Subsequently, this film was dissolved by dropwise addition of 12 mL of a phosphate-buffered saline (PBS) solution containing 100ug/mL DOX. The film was completely dissolved using ultrasonic agitation for 5 minutes. The preparation was then hydrated at 37 °C for an hour, cooled to 25 °C, and finally subjected to probe sonication in an ice bath for 2 minutes to produce the DOX@cRGD-Lip (DRL). A 1:1 volume ratio of BTNPs@DSPE-PEG NPs and DRL was combined and subjected to physical extrusion. This mixture was passed ten times through a 200 nm porous polycarbonate membrane, resulting in the formation of DBRL. Similar procedures were used to prepare BTNPs@cRGD-Lip (BRL). For Cy5.5-labeled DBRL NPs, the DSPE-Se-Se-PEG-NH_2 was substituted with an equivalent quantity of DSPE-PEG_{2000}-Cy5.5 for the formulation of liposomes. In addition, DSPE-PEG was used to replace DSPE-PEG-cRGD in the formulation of non-targeted liposomes. These liposomes were then formulated into DOX/BTNPs@Lip (DBL) and served as the control in cellular uptake assays.

Characterization of Nanoparticles

The observation of DBRL NPs was conducted using a transmission electron microscope (TEM) (JEM-2100Plus, Japan) operating at an accelerating voltage of 100 kV. The sample suspension, diluted with deionized water, was applied onto a copper grid coated with a carbon film. Subsequently, the dried samples were examined via TEM. The hydrodynamic diameters and zeta potential of the samples were measured using a Zetasizer Nano ZS (Malvern Instruments, UK) at 25 °C. Utilizing an X-ray diffraction system (Ultima IV X-ray diffractometer, Japan) with a Co Kα radiation source, the XRD patterns of the samples were obtained by scanning between 20° and 90° (2θ). Fourier transform infrared (FTIR) spectra were collected for the samples utilizing an FTIR spectrophotometer (Alpha type, Bruker, USA). The drug loading efficiency of DBRL NPs was measured through the UV−Vis method (Lambda 750s, PE instruments, USA).

In vitro Release of DOX

The in vitro drug release was assessed following established protocols.[33,34] NPs were suspended in PBS with 1% fetal bovine serum (FBS) at pH 5.5 and pH 7.4 in centrifuge tubes and placed in a shaking incubator at 37°C, with or without US (3 min at 0, 2, 4 h, total 3 times) (1.5 W/cm^2, 50% duty cycle, 1 MHz). Sampling was performed at designated time points (0.5, 1, 2, 4, 8, 12, and 24 hours) by exchanging 2 mL of PBS containing 1% FBS with an equivalent volume of fresh PBS. Subsequently, the concentrations of DOX released from the NPs were quantified using UV-Vis spectroscopy (Lambda 750s, PE Instruments, USA).

Hemolysis Test

The hemocompatibility of the nanoparticles was assessed through hemolysis testing. Blood samples were obtained from mice following the completion of other experimental procedures and immediately mixed with 3.8% sodium citrate anticoagulant solution. Following gentle inversion, the mixture was centrifuged (1000 g, 10 min) to separate blood components. After removing the plasma layer, erythrocytes were purified by three successive washing steps with isotonic saline (0.9% w/v). A standardized 2% (v/v) erythrocyte suspension was prepared for the hemolysis evaluation. The test samples (BRL, DRL and DBRL) were introduced to the erythrocyte suspension and maintained at 37 °C with gentle orbital shaking for 8 h. Sample tubes were then centrifuged (500 g, 5 min) to pellet intact cells. The extent of hemolysis was determined by measuring hemoglobin release in the supernatant using spectrophotometric analysis at 540 nm. Isotonic saline and 50% (v/v) deionized water served as the negative control and positive control, respectively. Hemolysis percentages were normalized to the maximum lysis control. All assays were conducted in triplicate.

Detection of ROS Generation

DPBF was employed as the molecular probe to identify ROS. The combination of NP and DPBF was exposed to 3 minutes of ultrasonic irradiation (1.5 W/cm², 50% duty cycle, 1 MHz) in the absence of light. Subsequently, UV-Vis spectra were obtained at specific time points (0, 1, 3, 7, 13, and 21 hours).

Cellular Uptake

MDA-MB-231 human breast cancer cells, MCF-10A human mammary epithelial cells, 4T1 mouse breast cancer cells, and RAW 264.7 mouse macrophage cells were obtained from Procell Life Science & Technology Co., Ltd. (Wuhan, China).

4T1 and RAW264.7 cells were seeded at a density of 5×10^5/mL in 24-well plates, with 1 mL per well, and allowed to adhere overnight. Subsequently, an equivalent amount of DBL and DBRL NPs was introduced into the culture medium. The cells were then co-incubated for 4 hours with or without US (1MHz, 1.5 W/cm^2, 50% duty cycle) for varying durations. Following this, the cells were washed, fixed, and their nuclei were stained with Hoechst 33342 at 25 °C. The uptake of DBL and DBRL by RAW264.7 and 4T1 cells was assessed using a laser confocal microscope.

ROS Detection in vitro

ROS generation was quantified using dichloro-dihydro-fluorescein diacetate (DCFH-DA) upon US irradiation. The ROS Assay Kit procured from Beyotime Biotechnology was utilized. Various experimental groups (PBS, US, DOX, BRL, DRL, DBRL, BRL + US, DBRL + US) were established to assess ROS production capacity, with the PBS group designated as the control. 4T1 cells (5×10^5 cells per well) were cultured in a 24-well plate. After a 24-hour incubation period, DOX, BRL, DRL, and DBRL (at a BTNPs equivalent concentration of 100 μg/mL) were added to the wells and incubated for an additional 4 hours. Then, the cells were subjected to US irradiation (1.5 W/cm^2, 50% duty cycle, 1 MHz) for 3 minutes. The medium was then aspirated and DCFH-DA was added to the wells and co-incubated for an additional 20 minutes. Fluorescence imaging was conducted using a fluorescence microscope. Each experiment was independently replicated three times. The fluorescence signal intensity correlated with the cellular ROS levels.

Cytotoxicity

To evaluate the cytotoxicity of DBRL nanoparticles, cell viability was measured using the standard Cell Counting Kit-8 (CCK-8) assay. Firstly, MCF-10A cells were seeded in a 96-well culture plate at a density of 10^4 cells/well and incubated for 24 h. Then, the cells were co-cultured with DBRL medium (0, 50, 100, 200, and 400 μg/mL, n=5) for 24 h. Finally, the cell viability was measured on a microplate reader (iMark, BIO-RAD).

To evaluate cytotoxicity, 4T1 cells and MDA-MB-231 cells were seeded at a density of 1×10^4 cells per well in 96-well plates and cultivated overnight in 1640 medium with 10% FBS. Subsequently, the cells were subjected to various treatments for 24 hours, with or without US (1.0 MHz, 1.5 W cm^2, 50% duty) for 3 minutes. Cell viability was determined 24 hours post-treatment using the CCK-8 assay, with free DOX (5ug/mL), DRL NPs, and BRL NPs serving as controls.

To visualize cytotoxicity effects, 4T1 cells were seeded at a density of 5×10^4 cells per well in 24-well plates and exposed to DBRL NPs (100 μg/mL BTNPs) for 24 hours. Subsequent to a 3-minute US irradiation session (1.0 MHz, 1.5 W/cm^2, 50% duty cycle), the cells were further incubated for 24 hours. After staining with Calcein-AM/PI solution, fluorescence imaging was performed utilizing a fluorescence microscope (Leica, Germany). Free DOX, DRL NPs, and BRL NPs were included as controls.

To study the effects of DBRL NPs on cellular apoptosis, 4T1 cells were seeded at a density of 5×10^4 cells per well in 24-well plates and grown overnight. The cells were treated with DBRL NPs (100 μg/mL BTNPs) for 24 hours, followed by 3 minutes of US irradiation (1.0 MHz, 1.5 W/cm2, 50% duty cycle) or left untreated. After a further 6 hours of incubation, the cells were treated with Annexin V/PI dye and flow cytometry was used to determine cell apoptosis.

ROS Detection in Tumor Tissues

To investigate ROS generation within tumors, Balb/c nude mice with 4T1 tumors were intravenously administered DBRL NPs at a dosage of 10.0 mg/kg BTNPs. Subsequently, the tumors were intratumorally injected with DHE, at a concentration of 10 μM in 50 μL. Following a 30-minute interval, the tumors were subjected to US irradiation (1MHz, 1.5 W/cm^2, 50% duty) for 10 minutes. The mice were then euthanized via cervical dislocation for tumor extraction. Tumor slices were acquired using cryosectioning, and fluorescence imaging was performed using a fluorescence microscope (Leica, Germany).

In vivo Toxicity Evaluation

The BALB/c nude mice were assigned randomly to four groups. All mice were killed on certain dates (day 1, day 7, and day 14 following the injection). Hematoxylin and eosin (H&E) staining was performed on the organs that were taken for histological examination, and blood samples were obtained for the purpose of conducting biochemical assessment.

In vivo Fluorescence Imaging and Distribution

Animal experiments were conducted in accordance with the guidelines and approval of the Animal Ethics Committee of Qingdao University (Approval No. QDUJ-AEC-2024465). Subcutaneous injection of 5×10^6 4T1 cells into 4–6-week-old BALB/c nude mice was utilized to establish a breast tumor model. Mice with a tumor volume of 150 mm^3 were selected for the experiment after 7 days. They were randomly divided into two groups (3 mice per group) for intravenous injection of DBRL-Cy5.5 and Free Cy5.5 via the tail vein. Fluorescence imaging was performed before treatment (at 0 h) and at 3 h, 6 h, 12 h, and 24 h post-treatment using IVIS Lumina III (PerkinElmer). Following imaging, all animals were euthanized, and major organs (heart, lung, liver, spleen, and kidney) along with tumor tissues were isolated and imaged using the same system.

In vivo Antitumor Therapy

Forty Balb/c nude mice, aged 4–6 weeks, were subcutaneously injected with 5×10^6 4T1 cells to establish a breast cancer model. Upon reaching a tumor volume of approximately 150 mm^3, the mice were randomly allocated into eight groups: (1) Control, (2) US, (3) DOX (5mg/kg), (4) BRL, (5) DRL, (6) DBRL, (7) BRL + US, (8) DBRL + US. NPs (10 mg/kg based on BTNPs), saline, or DOX were administered via the tail vein on days 1, 4, and 7. US irradiation (1.5 W/cm^2 for 3 minutes) was applied 12 hours post-injection. Throughout the study, body weight and tumor volume were monitored every other day using the formula: (width^2 × length) × 1/2. At the conclusion of the experiment, the mice were euthanized, and tumors were excised, weighed, and subjected to histological analysis through H&E and TdT-mediated dUTP Nick-End Labeling (TUNEL) staining.

Statistical Analysis

The data were presented in triplicate, unless otherwise noted. For in vitro studies, a minimum of three independent experiments were performed with technical triplicates. For in vivo studies, we determined that a minimum of 5 mice per group would be required to achieve statistical significance. The data were expressed as mean ± standard deviation (SD) values. For multiple group comparisons, the statistical significance between sample groups was assessed using a one-way ANOVA followed by Tukey's post hoc test. Two-way ANOVA was used for experiments involving two independent variables. The results were reported as follows: *$p < 0.05$; **$p < 0.01$, ***$p < 0.001$, ****$p < 0.0001$.

Results and Discussion

Fabrication and Characterization of DBRL Nanoparticles

Liposome NPs are widely acknowledged as efficient vehicles for delivering bioactive substances, commonly employed in controlled release mechanisms and tissue repair.[35] Our study focuses on the creation of a ROS-responsive liposome with a "Se-Se" structure using the thin-film hydration method (Figure 2A). Upon synthesizing the blank liposome cRGD-Lip (RL), DOX was encapsulated in the hydrophilic layer of the liposome, leading to the creation of DRL. DRL and BTNPs

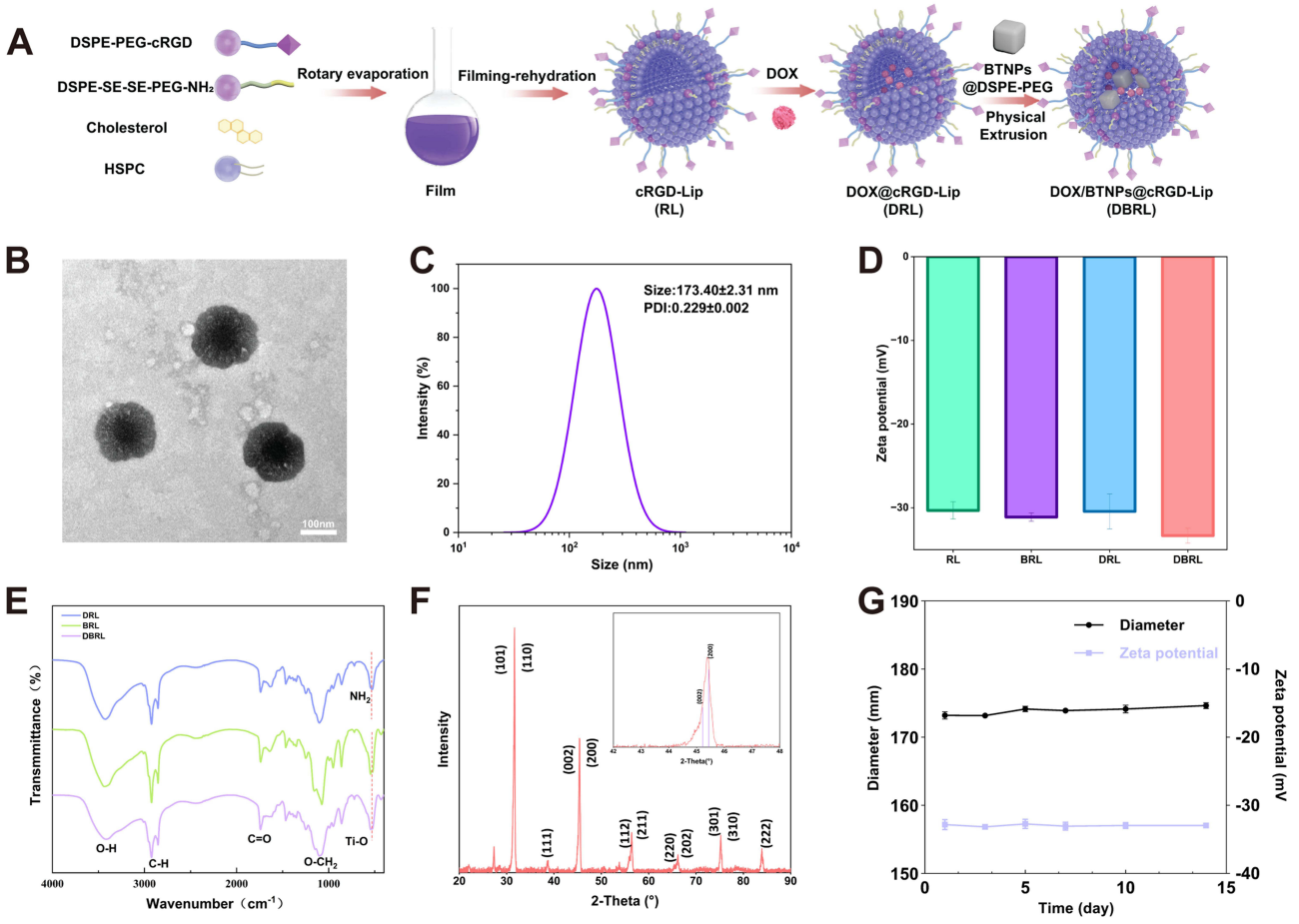

Figure 2 Fabrication and Characterization of DBRL NPs. (**A**) Schematic diagram of the DBRL NP preparation process. (**B**) Representative TEM images of DBRL NPs. (**C**) Size distribution of the DBRL NPs. (**D**) Zeta potential measurements of RL, BRL, DRL, and DBRL NPs. (**E**) FTIR spectra of BRL, DRL, and DBRL NPs. (**F**) XRD patterns of DBRL NPs. (**G**) Hydrodynamic sizes and zeta potentials of the DBRL NPs were measured after storage at 37 °C for 14 days.

were assembled to produce DBRL. The production of DBRL NPs included the usage of tetragonal BTNPs, known for their piezocatalytic properties,[27] confirmed through X-ray diffraction analysis (XRD) (Figure S1). These NPs exhibit the capability to generate ROS upon interaction with water under US exposure.[36] To evaluate the successful formulation of DBRL NPs, TEM was employed for morphological characterization. The TEM image distinctly revealed that the DBRL exhibited a uniform spherical morphology with an average diameter of approximately 180 nm (Figure 2B), which was well consistent with the dynamic light scattering (DLS) measurement (Figure 2C). The particle size distribution of DBRL was 0.229 ± 0.002, suggesting a monodisperse structure in aqueous solution. The zeta potential values of RL, BRL, DRL, and DBRL NPs were measured to be −30.30 ± 1.04 mV, −31.11 ± 0.50 mV, −30.42 ± 2.08 mV, and −33.32 ± 0.89 mV, respectively (Figure 2D). The negative charge of DBRL NPs contributed to their stability in aqueous solution. The FTIR spectroscopy reveals that the prominent peak at 3429 cm^{-1} corresponds to the -OH stretching vibration in lipids or DOX. The weak double peak at 2848 cm^{-1} and 2948 cm^{-1} corresponds to the -C-H stretching vibration in the fat chain, while the peak at 1743 cm^{-1} is attributed to the C=O group stretching vibration. The 1464 cm^{-1} peak in DRL corresponds to the symmetrical -COO vibration. Additionally, the peak intensity of DBRL NPs at this position is due to the Ti-O bending vibration. The broad peak at 1087 cm^{-1} corresponds to the C-O-C stretching vibration, and the peak at 855 cm^{-1} is associated with the in-plane bending vibration of the epoxy compound. Finally, the peak at 530 cm^{-1} represents the -NH_2 stretching vibration in DRL and corresponds to the Ti-O stretching vibration in DBRL NPs (Figure 2E). XRD of the synthesized DBRL NPs revealed distinct peaks corresponding to the (110), (002), (200), (211), (220), and (310) crystal planes associated with BTNPs. Notably, the diffraction peaks observed at approximately 2θ = 45° for (002) and (200) indicated the tetragonal phase of the BTNPs (Figure 2F). Furthermore, the DBRL NPs exhibited an average diameter and

https://doi.org/10.2147/IJN.S505526

Zeta potential of 173.23 ± 0.541 nm and −32.81 ± 0.75, respectively, on day 1, and 174.64 ± 0.43 nm and −32.95 ± 0.34, respectively, on day 14 (Figure 2G). These measurements revealed no significant alterations in particle size and PDI following a 14-day storage period, underscoring the exceptional stability of DBRL NPs, likely attributed to its negative charge. The dispersion states of the DBRL NPs were examined in various media (PBS, saline, 1640, DMEM, and FBS) to assess their uniformity. Figure S2 illustrates that the DBRL NPs were uniformly dispersed in all media, indicating their suitability for in vivo studies. The encapsulation efficiency and drug loading content of DBRL NPs were quantified via the UV-vis method. DOX encapsulation efficiency in the DBRL NPs was determined to be 87.34%, with a drug loading content of 8.19%, demonstrating a significant level of drug loading efficiency. These findings all supported the effective manufacture of DBRL NPs. As a result, DBRL NPs made of DOX and BTNPs were synthesized as intended, demonstrating not only excellent size stability but also uniform nanoscale particle size, allowing for passive targeting of tumors via the EPR effect.

In order to assess the controlled release of DOX induced by US, DBRL was loaded into dialysis bags with a molecular weight cutoff of 7000 Da. The bags were then placed in a constant temperature shaker set at 37 °C and 120 rpm for further evaluation. The purpose of include FBS in the release medium was to create an environment that was similar to that of the blood in vivo.[37] The release rate of DOX was determined using UV-vis analysis. Upon ultrasonic stimulation, the in vitro drug release from the DBRL NPs showed a significant enhancement relative to the DRL NPs (Figure 3A). However, the drug release patterns of the DBRL NPs were similar under both neutral (pH 7.4) and acidic (pH 5.5) conditions (Figure 3B). This suggests that the phospholipid membrane effectively shielded the DBRL NPs from degradation in both physiological and acidic environments. Additionally, the in vitro experiments showed that all NPs exhibited excellent biocompatibility, with no observable hemolysis of red blood cells in their presence (Figure 3C).

The production of ROS plays a crucial role in SDT involving BNTPs sonosensitizers. The ability of DBRL NPs to generate ROS under ultrasound stimulation was assessed using DPBF. Following US exposure, the DPBF absorbance in the DBRL NPs solution steadily decreased to 64% of its initial value, indicating ROS production (Figure 3D). It is possible that the photodegradation and quenching of DPBF itself are responsible for the decrease in DPBF absorbance that occurred in the PBS and DRL groups after the treatment with ultrasonic stimulation. The enhanced DOX release from DBRL NPs under ultrasonic stimulation can be attributed to a dual-mechanism process. First, upon ultrasound irradiation, BTNPs generate ROS through piezoelectric effect-induced charge separation and subsequent reactions with surrounding water and oxygen molecules. The produced ROS then cleaves the ROS-sensitive Se-Se bonds in the liposomal membrane, leading to controlled destabilization of the lipid bilayer. Simultaneously, the mechanical effects of ultrasound cavitation may contribute to increased membrane permeability. This synergistic effect explains the significantly higher DOX release rate observed in DBRL+US group (64% release at 24h) compared to DBRL without US stimulation (28% release at 24h). The ROS-responsive nature of our delivery system is further validated by the similar release profiles under both neutral (pH 7.4) and acidic (pH 5.5) conditions, indicating that the drug release is primarily triggered by ROS rather than pH changes. This feature is particularly advantageous as it enables precise spatiotemporal control of drug release specifically at the tumor site through external ultrasound activation, while maintaining stable drug encapsulation during circulation. Moreover, the step-wise US application (3 min at 0, 2, 4 h) resulted in distinct burst releases following each stimulation, demonstrating the controllable nature of this release mechanism. This observation supports our design rationale of combining piezoelectric BTNPs with ROS-sensitive liposomes for on-demand drug delivery.

Cell Uptake and ROS Generation at the Cellular Level

To evaluate the tumor-targeting abilities of DBRL NPs in vitro, the NPs were separately exposed to two cell lines: 4T1 breast cancer cells and RAW264.7 macrophage cells. The fluorescence intensity was notably higher in 4T1 cells compared to RAW264.7 cells (Figure 4A). This may be attributed to the incorporation of polyethylene glycol in the DBRL. This disparity underscores DBRL's specific affinity for 4T1 cancer cells and its ability to circumvent macrophages, positioning it as a potential precision tool in cancer therapy. We conducted a comparative analysis of the cellular uptake efficacy of DBRL in contrast to DBL through fluorescence microscopy. Our findings revealed a notably elevated fluorescence intensity in 4T1 cells exposed to DBRL, as opposed to those treated with DBL. Conversely, in macrophages,

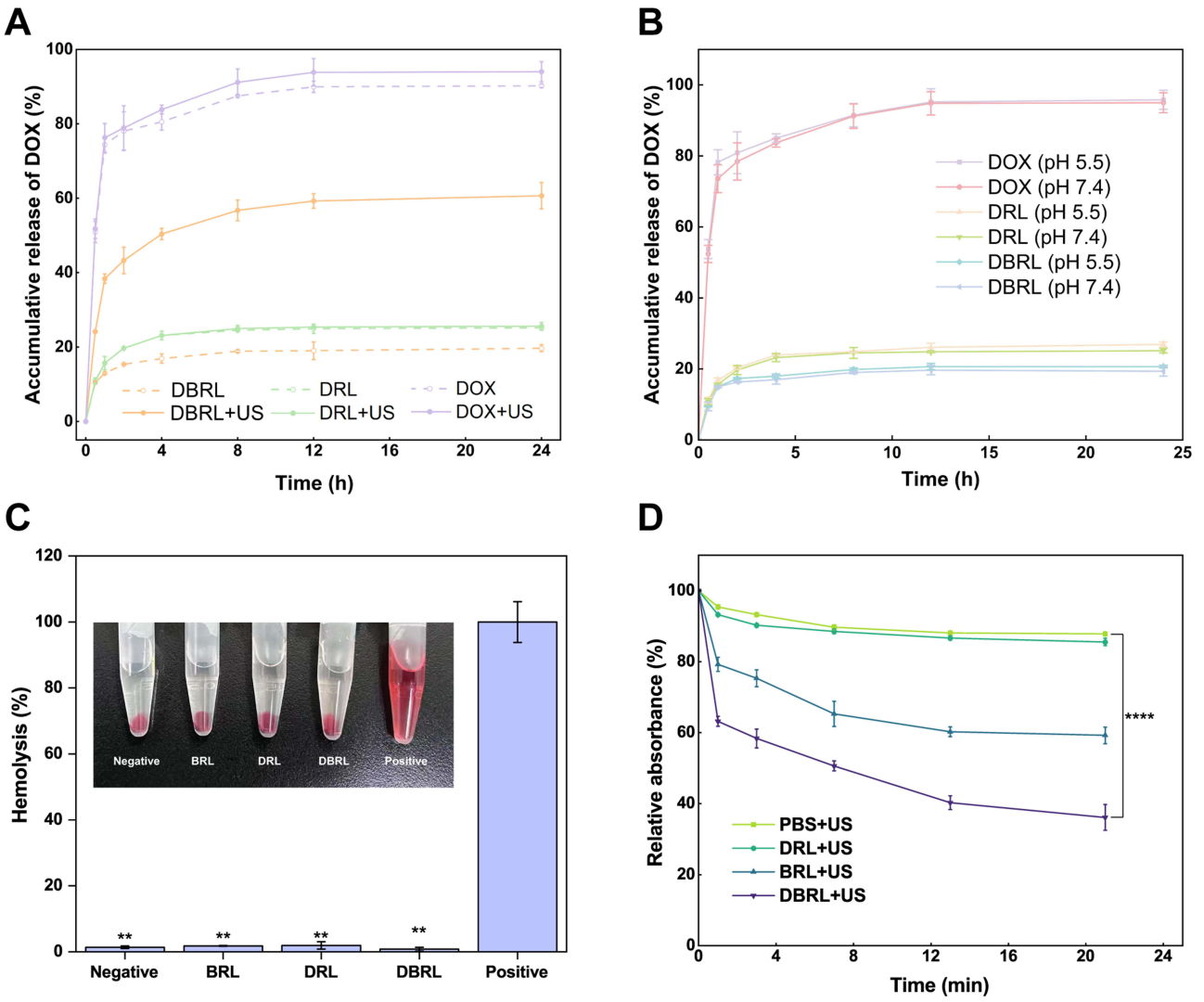

Figure 3 In vitro release, hemolysis studies, and ROS generation evaluation of NPs. (**A**) DOX release behaviors of various samples with or without US (3 min at 0, 2, 4 h, total 3 times) (US parameters: 1.0 MHz, 1.5/W cm^2, 50% duty). (**B**) DOX release behaviors of various samples in PBS containing 1% FBS (pH 5.5 and pH 7.4) for 24 h at 37 °C. (**C**) Photographs of 0.9% Saline, deionized water, BRL, DRL, and DBRL dispersed in 2% RBCs solution for 8h. (**D**) The ROS generation evaluation of NPs. Relative UV absorbance of DPBF in different solutions at 410 nm (PBS, BRL, DRL, DBRL) under the irradiation of US (1.0 MHz, 1.5 W/cm^2, 50% duty). Data were presented as mean ± standard deviation (SD) (n = 3).

DBL exhibited superior uptake efficiency compared to DBRL. This variance in uptake highlights the targeted specificity of DBRL NPs towards cancer cells (Figure 4A). Moreover, intracellular DOX release triggered lysosome escape as evidenced by confocal microscopy (Figure 4B). The observations revealed a gradual shift in the fluorescent patterns of lysosomes and DOX from colocalization to distinct localization following US irradiation. These findings demonstrate the US-induced release of DOX from DBRL NPs, facilitating subsequent escape of DOX from lysosomes to elicit its therapeutic effects.

The ROS generation capacity of DBRL in solution prompted an investigation into ROS production in tumor cells using fluorescent probes as indicators. Intracellular ROS production was assessed using DCFH-DA, which is non-fluorescent and is oxidized to form green fluorescent 2′,7′-dichlorofluorescein (DCF). Strong green fluorescence was observed only in the BRL + US and DBRL + US groups, with minimal fluorescence in other groups (Figure 4C). This suggests that ROS production at the cellular level is significantly enhanced only when BTNPs are combined with US, aligning well with the findings in solution (Figure 3D).

https://doi.org/10.2147/IJN.S505526

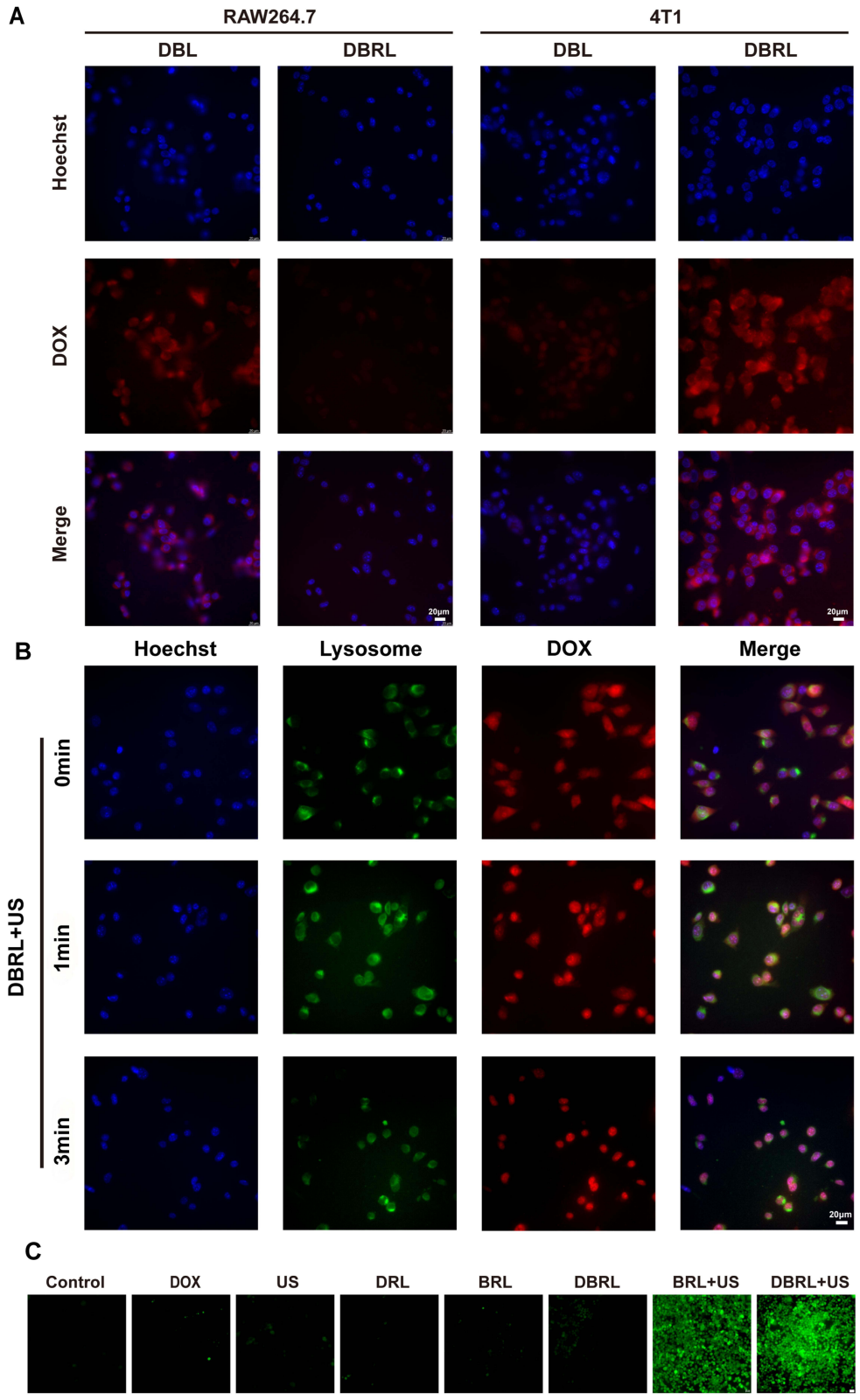

Figure 4 Cell Uptake and ROS Generation at the Cellular Level. (**A**) The fluorescent images of DBL and DBRL after co-incubation with RAW264.7 and 4T1 cells for 4 h, respectively. (**B**) Fluorescent images of 4T1 cells treated with DBRL for 4 h, followed by US irradiation (1MHz, 1.5 W/cm^2, 50% duty cycle) for different durations. (**C**) Detection of ROS by DCFH-DA in 4T1 cells under different treatments (scale bar: 100 μm; 100 μg/mL BTNPs for DBRL NPs; 1 MHz, 1.5 W/cm^2, 50% duty cycle, 3 min).

Synergistic Therapeutic Effect in vitro Against Tumor Cells

DBRL NPs showed negligible cytotoxicity to normal cells within the concentration range of 0 to 400 μg mL^{-1}. Although at the high concentration of 400 μg mL^{-1}, the viability of MCF-10A cells treated with DBRL NPs also reached over 90%, indicating the low cytotoxicity and excellent biocompatibility of DBRL NPs (Figure S3).

Significant cytotoxicity towards 4T1 cell lines was observed with DBRL NPs under US conditions, as shown by the CCK-8 assay (Figure 5A). Similarly, the CCK-8 results demonstrated significant cytotoxicity against another TNBC cell line, MDA-MB-231, further validating the broad therapeutic efficacy of DBRL NPs (Figure S4). Calcein-AM/PI costaining was then conducted after various treatments to directly see the killing impact of DBRL + US. Red fluorescence, with normalized fluorescence intensities of 52.84% and 55.70%, respectively, indicated cell death largely in the BRL + US and DBRL + US groups. These results were consistent with those reported with the CCK-8 test. Despite the presence of some dead cells, there were still numerous live cells (green fluorescence) in the DOX groups, indicating the restricted therapeutic efficacy of DOX (Figure 5B and C). To further verify the cellular damage caused by DBRL, Flow cytometry was used to measure the apoptotic rates of 4T1 cells in various treatment groups (Figure 5D). In comparison to the control group, the groups treated with US and BRL had apoptotic rates of less than 10%, while the DBRL + US group had a significantly higher apoptotic rate of 74.17% in 4T1 cells. The DBRL group had a rate of 21.12% and the BRL + US group had a rate of 52.88%. The better therapeutic efficacy of DBRL via US-induced piezocatalysis was confirmed by these results, which were in line with the Calcein-AM/PI costaining and CCK-8 test findings. The increased cellular uptake of DBRL not only facilitated ROS generation but also led to enhanced cancer cell death through the increased release of DOX in combination with SDT and chemotherapy. These results were supported by the findings of tumor cell uptake experiments and ROS generation in vitro.

In vivo Biocompatibility of DBRL

Before applying NPs in vivo, it was necessary to ensure good bio-compatibility. DBRL exhibited minimal cytotoxicity in cellular assays (Figure 5A); subsequently, its acute toxicity in blood and organ toxicity were assessed. DBRL was intravenously injected into healthy mice at a high concentration of 10 mg/kg BTNPs. On days 1, 7, and 14, blood samples were obtained for biochemical examination. The percentages of various indicators, such as white blood cells (WBC), red blood cells (RBC), platelets (PLT), hemoglobin (HGB), mean platelet volume (MPV), red blood cell volume distribution width (RDW), hematocrit (HCT), mean corpuscular volume (MCV), mean corpuscular hemoglobin concentration (MCHC), lymphocytes (Lymph), granulocytes (Gran), and monocytes (Mon), all exhibited comparable values as the PBS control for all three time points (Figure 6A). This shows that there was no acute toxicity induced by DBRL. The toxicity profiles of vital organs, including the heart, liver, spleen, lung, and kidney, were evaluated using H&E staining. The results demonstrated a lack of pathological changes or inflammation in the DBRL-treated group compared to the PBS-treated group (Figure 6B). These findings were consistent with predictions based on the constituents of DBRL, which consist of endogenous lipids known for their exceptional compatibility with biological systems. Consequently, DBRL exhibited significant biocompatibility and promising potential for in vivo tumor therapy.

In vivo Biodistribution and ROS Generation of DBRL

After confirming excellent in vivo biocompatibility, the tumor accumulation and retention properties of DBRL were assessed in 4T1 tumor-bearing nude mice. Cy5.5 labeling was achieved by incorporating DSPE-PEG_{2000}-Cy5.5 during preparation. DBRL-Cy5.5 was administered via tail vein injection to the mice, and fluorescence imaging was conducted at predetermined intervals (Figure 7A). Subsequent analysis revealed a gradual increase in fluorescence intensity at the tumor site post-injection, peaking at $(1.01 \pm 0.33)\times10^9$ at 12 hours and decreasing slightly to $(4.28\pm1.02)\times10^8$ at 24 hours (Figure 7B). These results suggest rapid tumor accumulation and prolonged retention of DBRL, indicating its potential for effective tumor therapy. Ex vivo imaging of dissected organs and tumor after 12 hours post-injection revealed strong fluorescence in the tumor, underscoring DBRL's favorable tumor accumulation capability. Additionally, prominent fluorescence signals in the liver and kidney indicated the primary sites for DBRL degradation and excretion (Figure 7C).

After confirming the targeted accumulation of DBRL NPs at the tumor site, we evaluated the in vivo generation of ROS using DHE in nude mice bearing 4T1 tumors (Figure 7D). Tumors were excised post-treatment, sectioned at their

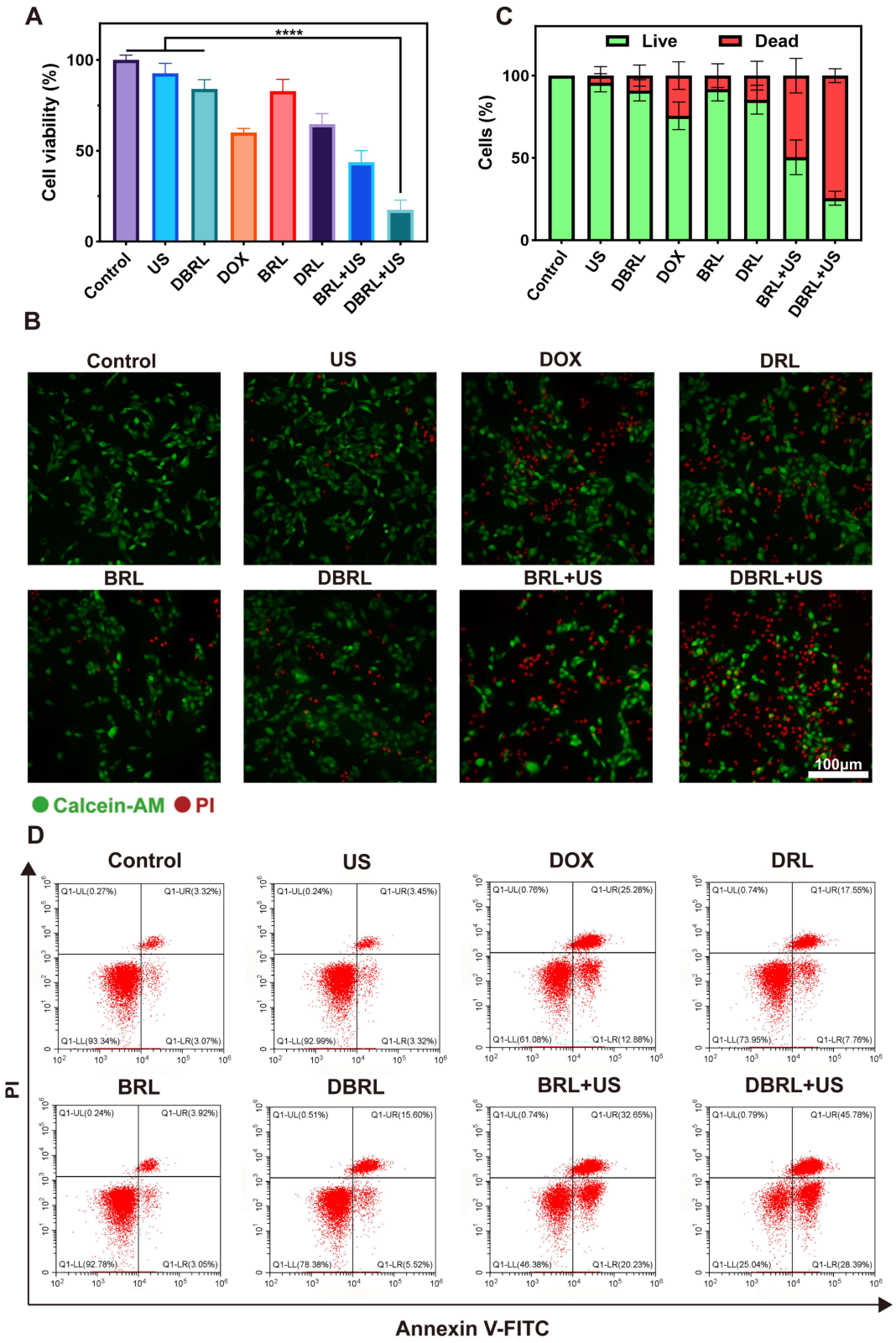

Figure 5 Synergistic therapeutic effect in vitro against tumor cells. (**A**) Cell viabilities of 4T1 cells under different treatments (n = 4). (**B**) 4T1 cells costained with Calcein-AM/PI after different treatments. (**C**) The quantitative analysis of Calcein-AM/PI fluorescence images of 4T1 tumor cells after different treatments. (**D**) 4T1 cells apoptosis analysis via flow cytometry (100 μg/mL BTNPs for DBRL NPs; 1 MHz, 1.5 W/cm^2, 50% duty cycle, 3 min; ****: $p < 0.0001$).

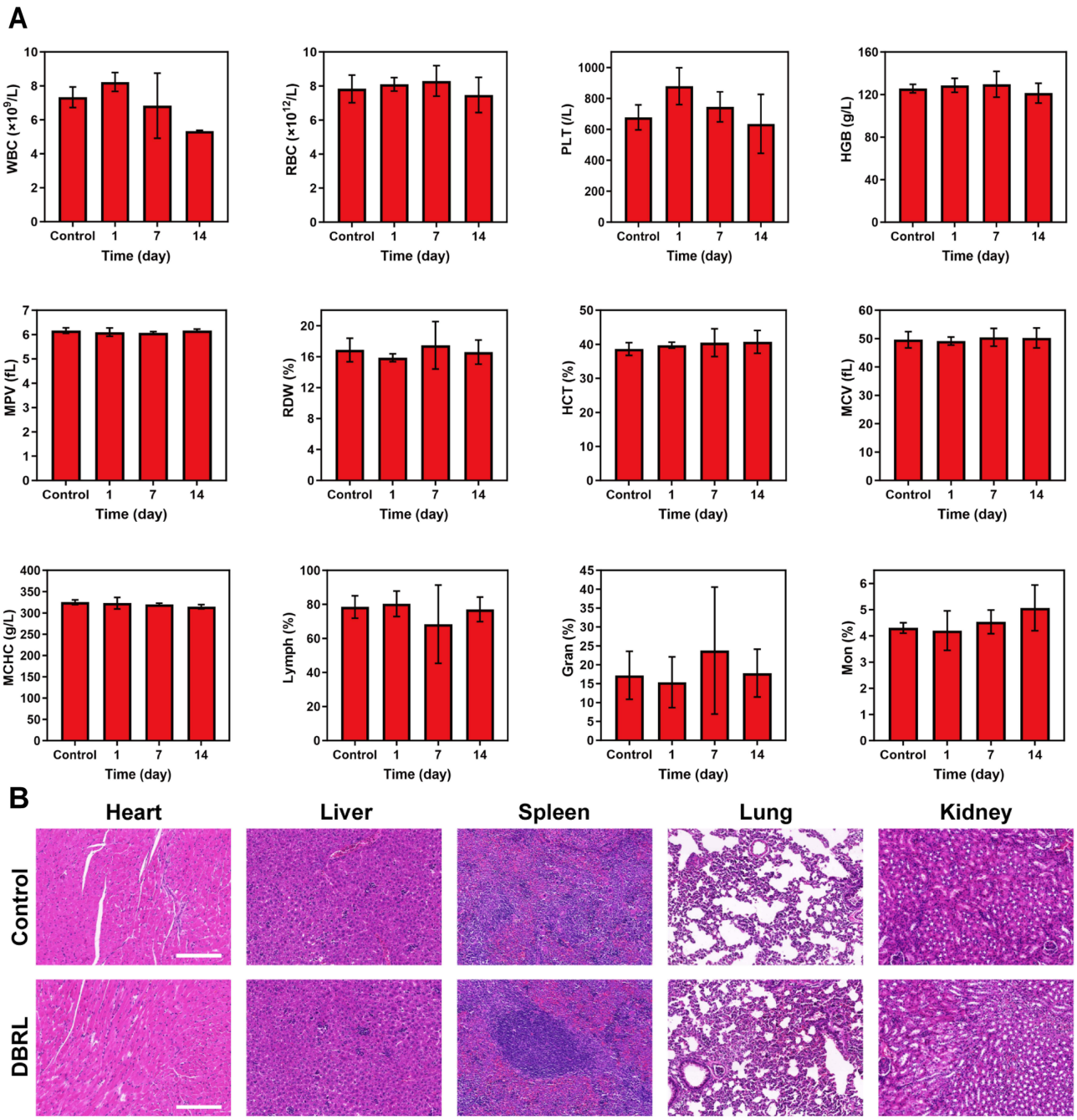

Figure 6 In vivo biocompatibility of DBRL. (**A**) The changes in WBC (/L), RBC (/L), PLT (/L), HGB (g/L), MPV (fL), RDW (%), HCT (%), MCV (fL), MCHC (g/L), Lymph (%), Gran (%), and Mon (%) counts at different times after injection of DBRL (10 mg/kg BTNPs) (n = 3). (**B**) H&E staining images of major organs at day 14 after injection of DBRL (10 mg/kg BTNPs); PBS-treated mice were used as a control (scale bar: 200 μm).

widest cross-section, and examined for fluorescence. Tumors treated with BRL and DBRL NPs in conjunction with US irradiation exhibited green fluorescence, indicating significant ROS levels. This observation suggests that ROS generation, likely originating from the encapsulated BTNPs, is consistent with previous reports of US-induced ROS production at the cellular level (Figure 4C). In contrast, DRL NPs did not show fluorescence when exposed to US irradiation at the tumor site, emphasizing the essential role of BTNPs in in vivo ROS generation upon US exposure to facilitate DOX release.

https://doi.org/10.2147/IJN.S505526

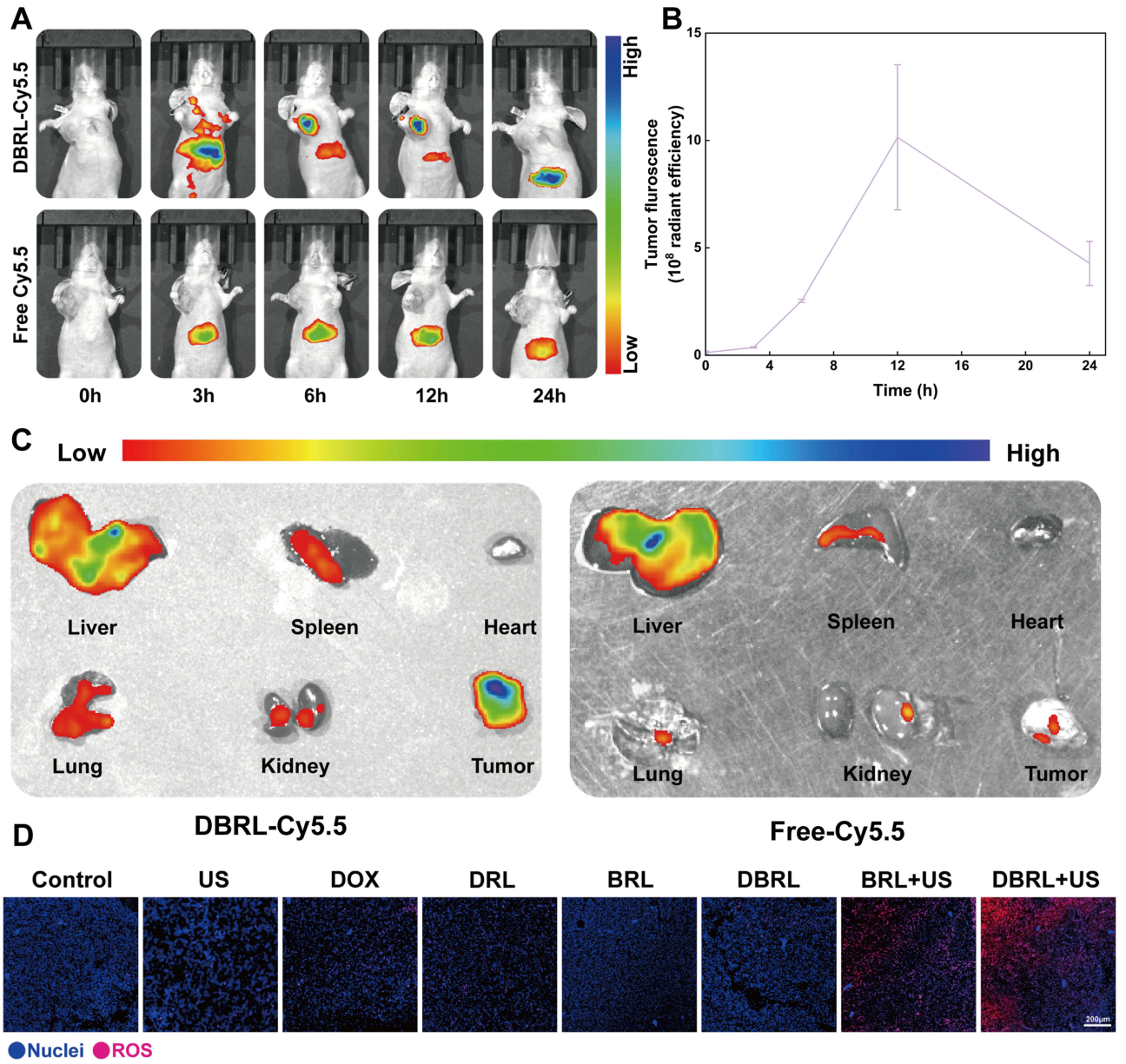

Figure 7 In vivo biodistribution and ROS generation in tumor tissues. (**A**) Dynamic fluorescence imaging of nude mice bearing 4T1 tumors after intravenous injection of DBRL-Cy5.5. (**B**) Quantification of dynamic fluorescence intensity in the tumor area (n = 3). (**C**) Fluorescence imaging of the main organs collected 12 hours post-injection of DBRL-Cy5.5. (**D**) ROS levels in 4T1 tumor tissues injected with different drugs in the presence or absence of US at 12 hours post-injection, using DHE as a probe.

In vivo Therapeutic Effect of DBRL

By utilizing US excitation, we explored the synergistic therapeutic effects of DBRL NPs in vivo on mice with 4T1 tumors. Figure 8A illustrates the process of tumor inoculation and treatment in a schematic form. Once the tumor volume reached approximately 150 mm^3 post-inoculation, a total of 40 nude mice were divided into eight groups, each designed to assess different therapeutic strategies and combinations. These groups included the Control group (receiving intravenous saline), US, DOX, DRL, BRL, DBRL, BRL + US, and DBRL + US. 10 minutes of US was administered to the US-related groups at the tumor site 12 hours after injection. The mice received treatments on days 1, 4, and 7, and their tumor volumes were monitored every two days, in addition to weighing the mice. As anticipated, the tumor volume (Figure 8B) at the conclusion of the experiments revealed that the Control, US, and BRL groups exhibited rapid tumor growth, reaching a final volume of around 1500 mm^3 by day 14, indicating that US or BRL alone did not have any therapeutic impact on the tumor. Conversely, some inhibitory effects were noted for the DOX, DRL, and DBRL treated groups. The

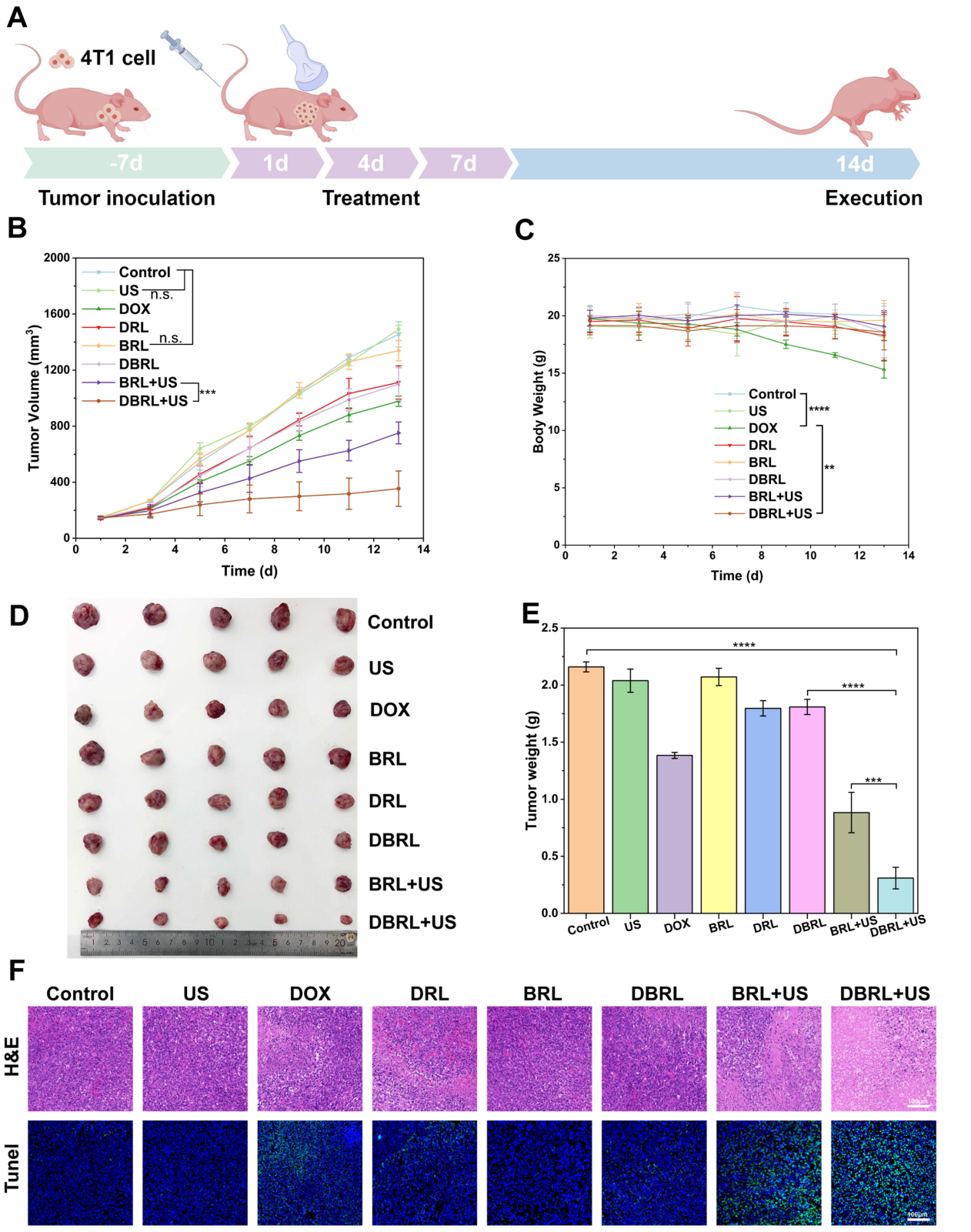

Figure 8 In vivo therapeutic effect. (**A**) Schematic illustration of treatment process. (**B**) Tumor volume change of 4T1 tumor-bearing nude mice in different groups. (**C**) Body weight change of 4T1 tumor-bearing nude mice during 14 days of treatment. (**D**) Photograph of the tumor extracted at the end of experiment. (**E**) Tumor weight of mice treated with different formulations. (**F**) Tumor tissues examined by H&E and TUNEL assay in different groups after 14 days of treatment (BTNPs dose: 10.0 mg/kg; US parameters: 1.0 MHz, 1.5 W/cm^2, 50% duty, 10 min). Data were presented as mean ± standard deviation (SD) (n = 5). ** p < 0.01, *** p < 0.001, ****P < 0.0001, Two-way ANOVA.

https://doi.org/10.2147/IJN.S505526

most effective treatment was evidently the combination of ROS and DOX, The DBRL + US group obtained a considerable inhibition rate of 70.27%, demonstrating good performance. Under US irradiation, BTNPs interacts with ambient water to generate ROS, which in turn triggers a massive release of DOX from the DBRL, resulting in the most effective destruction of tumor cells. The tumor tissues and main organs are taken from the mice after they have been killed on the fourteenth day of the experiment. The tumor tissues are imaged and weighed. In comparison to all other groups, the tumor in the DBRL + US group is the lightest (Figure 8D and E). Moreover, the body weight change curves of the mice and the histological examination of heart, liver, spleen, lung, and kidney tissues using HE staining indicated insignificant cardiotoxicity and no treatment-related side effects (Figure 8C) (Figure S3).

In order to uncover the antitumor mechanisms of DBRL under US irradiation more comprehensively, H&E and TUNEL staining were conducted on tumor tissues. Varied levels of tumor nuclei reduction and fragmentation were seen in the DOX, DRL, DBRL, BRL + US, and DBRL + US treated groups based on the H&E data. The order of damage severity was found to be DBRL < DRL < BRL + US < DBRL + US, which was consistent with their antitumor effects, as illustrated in Figure 8E. The TUNEL assay revealed that the DBRL + US group displayed the strongest green fluorescence, signifying a heightened level of cell apoptosis (Figure 8F). This observation further supports the notion that the enhanced cytotoxicity of DOX was potentiated and synergistically amplified by US-induced piezocatalysis based on BTNPs.

While our study demonstrates the efficacy of DBRL-mediated ROS generation for TNBC treatment, we acknowledge that potential resistance mechanisms and long-term ROS effects warrant careful consideration. Cancer cells may develop adaptive responses to oxidative stress through multiple cellular mechanisms. First, in response to chronic ROS exposure, tumor cells could upregulate antioxidant defense systems, particularly through activation of the Nrf2 pathway and increased expression of antioxidant enzymes such as superoxide dismutase and catalase. However, our pulsed ultrasound activation strategy may help circumvent this adaptation by providing intermittent rather than continuous ROS exposure. Second, the ROS generated by our system may also influence the tumor microenvironment. While acute ROS production effectively kills cancer cells, long-term oxidative stress could potentially modulate immune responses and affect stromal cells. Future studies investigating these aspects over extended periods would be valuable for optimizing treatment protocols. Third, we have considered the possibility of DOX resistance development. The combination of chemotherapy with ROS-mediated therapy may actually help overcome traditional drug resistance mechanisms, as ROS can disrupt multiple cellular pathways simultaneously. This multi-modal approach could reduce the likelihood of resistance development compared to single-agent treatments. We believe these considerations provide important context for the clinical translation of our therapeutic strategy.

Conclusions

Our findings demonstrate the successful development of a targeted drug delivery system that effectively addresses key challenges in TNBC treatment. The significant tumor inhibition rate achieved by DBRL+US, combined with excellent biocompatibility and selective cytotoxicity, underscores the therapeutic potential of this approach. The US-triggered ROS generation serves multiple functions: directly inducing cancer cell death, triggering DOX release, and potentially sensitizing tumor cells to chemotherapy.

From a clinical perspective, several aspects of our system show promise for translation. The US parameters used align with clinically approved ranges, suggesting feasibility for clinical implementation. Our 14-day biosafety study, showing no significant adverse effects on major organs or blood parameters, provides preliminary support for the long-term safety profile of DBRL. However, potential resistance mechanisms to ROS-based therapies, such as upregulation of antioxidant defenses or adaptive responses in tumor cells, warrant further investigation in future studies. The ROS-responsive drug release mechanism addresses a critical challenge in current TNBC therapy by enabling precise spatiotemporal control of drug delivery, which may help mitigate resistance development.

Furthermore, the enhanced tumor accumulation demonstrated by our biodistribution data, with peak fluorescence intensity at 12 hours post-injection, suggests the potential for improved therapeutic outcomes in clinical settings. These features, combined with the non-invasive nature of US activation, position this platform as a promising approach for integrating into existing TNBC treatment protocols. Future studies should focus on optimizing treatment regimens, evaluating long-term safety, and exploring potential synergies with standard therapies to maximize clinical relevance.

Data Sharing Statement

Data will be made available on request.

Acknowledgments

This work was supported by the Natural Science Foundation of Shandong Province under Grant [ZR2021MH403].

Disclosure

The authors declare that they have no known competing financial interests or personal relationships that could have appeared to influence the work reported in this paper.

References

1. Lin NU, Claus E, Sohl J, Razzak AR, Arnaout A, Winer EP. Sites of Distant Recurrence and Clinical Outcomes in Patients With Metastatic Triple-negative Breast Cancer High Incidence of Central Nervous System Metastases. *Cancer*. 2008;113:2638–2645.
2. Zhang L, Fang C, Xu XQ, Li AL, Cai Q, Long XH. Androgen Receptor, EGFR, and BRCA1 as Biomarkers in Triple-Negative Breast Cancer: a Meta-Analysis. *Biomed Res Int*. 2015;2015:12.
3. Dent R, Trudeau M, Pritchard KI, et al. Triple-negative breast cancer: clinical features and patterns of recurrence. *Clin Cancer Res*. 2007;13 (15):4429–4434.
4. Rouzier R, Perou CM, Symmans WF. Breast cancer molecular subtypes respond differently to preoperative chemotherapy. *Clin Cancer Res*. 2005;11(16):5678–5685. doi:10.1158/1078-0432.CCR-04-2421
5. Carey LA, Dees EC, Sawyer L. The triple negative paradox: primary tumor chemosensitivity of breast cancer subtypes. *Clin Cancer Res*. 2007;13 (8):2329–2334. doi:10.1158/1078-0432.CCR-06-1109
6. Liedtke C, Mazouni C, Hess KR. Response to neoadjuvant therapy and long-term survival in patients with triple-negative breast cancer. *J Clin Oncol*. 2008;26(8):1275–1281. doi:10.1200/JCO.2007.14.4147
7. Waks AG, Winer EP. Breast Cancer Treatment. *A Review JAMA*. 2019;321(3):288–300. doi:10.1001/jama.2018.19323
8. Kremer LCM, van Dalen EC, Offringa M, Voûte PA. Frequency and risk factors of anthracycline-induced clinical heart failure in children:: a systematic review. *Ann Oncol*. 2002;13(4):503–512. doi:10.1093/annonc/mdf118
9. Elliott P. Pathogenesis of cardiotoxicity induced by anthracyclines. *Semin Oncol*. 2006;33:S2–S7. doi:10.1053/j.seminoncol.2006.04.020
10. Longhi A, Ferrari S, Bacci G, Specchia S. Long-term follow-up of patients with doxorubicin-induced cardiac toxicity after chemotherapy for osteosarcoma. *Anti-Cancer Drugs*. 2007;18(6):737–744. doi:10.1097/CAD.0b013e32803d36fe
11. Nedeljkovic M, Damjanovic A. Mechanisms of Chemotherapy Resistance in Triple-Negative Breast Cancer-How We Can Rise to the Challenge. *Cells*. 2019;8(9):32. doi:10.3390/cells8090957
12. Wen LJ, Wang YS, Zhang J. Nano-gold micelles loaded Dox and Elacridar for reversing drug resistance of breast cancer. *IET Nanobiotechnol*. 2023;17(2):49–60. doi:10.1049/nbt2.12102
13. Rivankar S. An overview of doxorubicin formulations in cancer therapy. *J Canc Res Ther*. 2014;10(4):853–858. doi:10.4103/0973-1482.139267
14. Lorusso D, Di Stefano A, Carone V, Fagotti A, Pisconti S, Scambia G. Pegylated liposomal doxorubicin-related palmar-plantar erythrodysesthesia (‘hand-foot’ syndrome. *Ann Oncol*. 2007;18(7):1159–1164. doi:10.1093/annonc/mdl477
15. Jain V, Kumar H, Anod HV. A review of nanotechnology-based approaches for breast cancer and triple-negative breast cancer. *J Control Release*. 2020;326:628–647. doi:10.1016/j.jconrel.2020.07.003
16. Owens DE, Peppas NA. Opsonization, biodistribution, and pharmacokinetics of polymeric nanoparticles. *Int J Pharm*. 2006;307(1):93–102. doi:10.1016/j.ijpharm.2005.10.010
17. Peer D, Karp JM, Hong S, FaroKhzad OC, Margalit R, Langer R. Nanocarriers as an emerging platform for cancer therapy. *Nat Nanotechnol*. 2007;2(12):751–760. doi:10.1038/nnano.2007.387
18. Shi Y, Van der Meel R, Chen XY, Lammers T. The EPR effect and beyond: strategies to improve tumor targeting and cancer nanomedicine treatment efficacy. *Theranostics*. 2020;10(17):7921–7924. doi:10.7150/thno.49577
19. Hashida M. Advocation and advancements of EPR effect theory in drug delivery science: a commentary. *J Control Release*. 2022;346:355–357. doi:10.1016/j.jconrel.2022.04.031
20. Clemons TD, Singh R, Sorolla A, Chaudhari N, Hubbard A, Iyer KS. Distinction Between Active and Passive Targeting of Nanoparticles Dictate Their Overall Therapeutic Efficacy. *Langmuir*. 2018;34(50):15343–15349. doi:10.1021/acs.langmuir.8b02946
21. Kiran A, Kumari GK, Krishnamurthy PT, Khaydarov RR. Tumor microenvironment and nanotherapeutics: intruding the tumor fort. *Biomater Sci*. 2021;9(23):7667–7704. doi:10.1039/D1BM01127H
22. Gajbhiye KR, Gajbhiye V, Siddiqui IA, Gajbhiye JM. cRGD functionalised nanocarriers for targeted delivery of bioactives. *J Drug Target*. 2019;27 (2):111–124. doi:10.1080/1061186X.2018.1473409
23. Liu CY, Zhao WL, Zhang LG, Sun HM, Chen X, Deng N. Preparation of DSPE-PEG-cRGD Modified Cationic Liposomes for Delivery of OC-2 shRNA and The Antitumor Effects on Breast Cancer. *Pharmaceutics*. 2022;14(10):20. doi:10.3390/pharmaceutics14102157
24. Mirhadi E, Mashreghi M, Maleki MF, et al. Redox-sensitive nanoscale drug delivery systems for cancer treatment. *Int J Pharm*. 2020;589:18. doi:10.1016/j.ijpharm.2020.119882
25. Browning RJ, Able S, Ruan JL, et al. Combining sonodynamic therapy with chemoradiation for the treatment of pancreatic cancer. *J Control Release*. 2021;337:371–377. doi:10.1016/j.jconrel.2021.07.020
26. Dai ZJ, Li S, Gao J, et al. Sonodynamic therapy (SDT): a novel treatment of cancer based on sonosensitizer liposome as a new drug carrier. *Med Hypotheses*. 2013;80(3):300–302. doi:10.1016/j.mehy.2012.12.009

27. Zhu P, Chen Y, Shi JL. Piezocatalytic Tumor Therapy by Ultrasound-Triggered and $BaTiO_3$-Mediated Piezoelectricity. *Adv Mater*. 2020;32(29):8. doi:10.1002/adma.202001976
28. Tang QS, Sun SH, Wang P, et al. Genetically Engineering Cell Membrane-Coated BTO Nanoparticles for MMP2-Activated Piezocatalysis-Immunotherapy. *Adv Mater*. 2023;35(18):19. doi:10.1002/adma.202300964
29. Wang P, Tang QS, Zhang LL, et al. Ultrasmall Barium Titanate Nanoparticles for Highly Efficient Hypoxic Tumor Therapy via Ultrasound Triggered Piezocatalysis and Water Splitting. *ACS Nano*. 2021;15(7):11326–11340. doi:10.1021/acsnano.1c00616
30. Wang Y, Tang QS, Wu RQ, et al. Ultrasound-Triggered Piezocatalysis for Selectively Controlled NO Gas and Chemodrug Release to Enhance Drug Penetration in Pancreatic Cancer. *ACS Nano*. 2023;17:3557–3573.
31. Huang RH, Sobol NB, Younes A, et al. Comparison of Methods for Surface Modification of Barium Titanate Nanoparticles for Aqueous Dispersibility: toward Biomedical Utilization of Perovskite Oxides. *ACS Appl Mater Interfaces*. 2020;12(46):51135–51147. doi:10.1021/acsami.0c10063
32. Tang Q, Wang Y, Wu R, et al. Spatial-temporal-controlled NO gas and PARP1 siRNA delivery for alleviating the dilemma of deeper sonodynamic therapy in pancreatic cancer. *Chem Eng J*. 2024;490:151775. doi:10.1016/j.cej.2024.151775
33. Gao HY, Bai Y, Chen LJ, Fakhri GE, Wang MY. Self-Assembly Nanoparticles for Overcoming Multidrug Resistance and Imaging-Guided Chemo-Photothermal Synergistic Cancer Therapy. *Int J Nanomed*. 2020;15:809–819. doi:10.2147/IJN.S232449
34. Ye SF, Wang FF, Fan ZX, et al. Light/pH-Triggered Biomimetic Red Blood Cell Membranes Camouflaged Small Molecular Drug Assemblies for Imaging-Guided Combinational Chemo-Photothermal Therapy. *ACS Appl Mater Interfaces*. 2019;11(17):15262–15275. doi:10.1021/acsami.9b00897
35. Wu SL, Zhang H, Wang SC, et al. Ultrasound-triggered in situ gelation with ROS-controlled drug release for cartilage repair. *Mater Horizons*. 2023;10(9):3507–3522. doi:10.1039/D3MH00042G
36. Su R, Hsain AL, Wu M, et al. Nano-Ferroelectric for High Efficiency Overall Water Splitting under Ultrasonic Vibration. *Angew Chem Int Edit*. 2019;58(42):15076–15081. doi:10.1002/anie.201907695
37. Zhang WY, Han B, Gao CY, et al. Integrated platform of oxygen self-enriched nanovesicles: SP94 peptide-directed chemo/sonodynamic therapy for liver cancer. *Eur J Pharm Biopharm*. 2022;179:206–220. doi:10.1016/j.ejpb.2022.09.012